# Close Cassini Flybys of Saturn's ring moons Pan, Daphins, Atlas, Pandora, and Epimetheus

B. J. Buratti[1], P. C. Thomas[2], E. Roussos[3], C. Howett[4], M. Seiß[5], A. R. Hendrix[6], P. Helfenstein[2], R. H. Brown[7], R. N. Clark[6], T. Denk[8], G. Filacchione[9], H. Hoffmann[5], G. H. Jones[10], N. Khawaja[11], P. Kollmann[12], N. Krupp[3], J. Lunine[2], T. W. Momary[1], C. Paranicas[13], F. Postberg[12], M. Sachse[5], F. Spahn[5], J. Spencer[4], R. Srama[13], T. Albin[13], K. H. Baines[1], M. Ciarniello[9], T. Economou[14], S. Hsu[15], S. Kempf[15], S. M. Krimigis[12], D. Mitchell[12], G. Moragas-Klostermeyer[13], P. D. Nicholson[2], C. C. Porco[16], H. Rosenberg[8], J. Simolka[13], L. A. Soderblom[17]

[1]Jet Propulsion Laboratory, California Institute of Technology, Pasadena, CA 91109
[2]Department of Astronomy, Cornell University, Ithaca, NY 14853
[3]Max Planck Institute for Solar System Research, 37077 Göttingen, Germany
[4]Southwest Research Institute, Boulder, CO 80302
[5]Department of Physics and Astronomy, University of Potsdam, 14476 Potsdam, Germany
[6]Planetary Sciences Institute, Tucson, AZ 85719
[7]Lunar and Planetary Lab, University of Arizona, Tucson, AZ 85721
[8]Freie Universität Berlin, 12249 Berlin, Germany
[9]Istituto di Astrofisica e Planetologia, Via Fosso del Cavaliere 100, Rome, Italy
[10]University College London, London, UK
[11]Institut für Geowissenschaften, Universität Heidelberg, 69120 Heidelberg, Germany
[12]Applied Physics Laboratory, Johns Hopkins University, Laurel, MD 20723
[13]University of Stuttgart, Pfaffenwaldring 29, 70569 Stuttgart, Germany
[14]Enrico Fermi Institute, University of Chicago, Chicago, IL, 60637, USA
[15] Physics Department, University of Colorado, Boulder, CO 80303, USA
[16]Space Sciences Institute, Boulder CO 80301
[17]United States Geological Survey, Flagstaff, AZ 86001



Submitted to Science Feb. 6 for the Cassini End-of-Mission special issue
Resubmitted May 24, 2018; accepted March 12, 2019

**Saturn's main ring system is associated with a set of small moons that either are embedded within it or interact with the rings to alter their shape and composition. Five close flybys of the moons Pan, Daphnis, Atlas, Pandora, and Epimetheus were performed between December 2016 and April 2017 during the ring-grazing orbits of the Cassini mission. Data on the moons' morphology, structure, particle environment, and composition were returned, along with images in the ultraviolet and thermal infrared. We find that the optical properties of the moons' surfaces are determined by two competing processes: contamination by a red material formed in Saturn's main ring system and accretion of bright icy particles or water vapor from volcanic plumes originating on the moon Enceladus.**

## Introduction

Saturn possesses a family of small inner irregular moons that orbit close to its rings. Two moons orbit in gaps within Saturn's main ring system: Daphnis, which dwells in the A-ring's Keeler Gap (1), and Pan, which is found in the Encke Gap, also in the A-ring (2). Three others, called shepherd moons, orbit at the edges of the A-ring (Atlas) or the F-ring (Pandora and Prometheus) (3) (fig. S2). The co-orbital moons Janus and Epimetheus share horseshoe orbits outside the F-ring and swap their positions every 4 years (fig. S2). Saturn's rings are almost certainly tied to the origin and continued existence of these moons (1). It remains unclear whether the rings formed from the breakup of an inner moon, or whether the present ring moons formed from the consol-idation of existing ring material, either primor-dial or impact-created. The alteration processes acting on these moons and the rings, past and present, are also unknown.

Prior to Saturn's exploration by spacecraft, the main rings were thought to be unconsolidated primordial debris, unable to form a moon be-cause of tidal forces (4, 5). Evidence from the two Voyager spacecraft suggested that the rings and inner moons constituted debris from the break-up of a single parent body, or perhaps several parent bodies, with the moons being the largest fragments (4). Measurement of the rings' and moons' bulk densities using Cassini data (5), along with dynamical studies and the existence of ridges around the equators of Atlas and Pan (5, 6), suggested a more complicated, multistage formation. The ring moons—from Pan out to Pan-dora, but possibly also Janus and Epimetheus—likely formed from the very early accretion of low-density debris around a denser seed, pre-sumably a collisional shard from the breakup of a preexisting moon (5). In the cases of Atlas and Pan, this was followed by a second stage of accretion of material onto the equator, after the rings had settled into their present very thin disk (6, 7). In this scenario, the surfaces of these moons should be similar in composition to the rings.

Analysis of the optical properties of the moons, including color, albedo, and spectral properties in the visible and infrared between 0.35 and 5.2 mm, has shown that they resemble the ring sys-tems in which they are embedded or which they abut (8–11). An unidentified low-albedo reddish material that could be organic molecules, silicates, or iron particles (9–12) appears to be abundant in theringsandhasalsotingedthemoons(8–12), further supporting a common origin and imply-ing continuing accretion of particles onto the moons' surfaces. The interactions of the ring system with the inner moons may form two distinct zones: an inner region in the vicinity of the main ring system that is dominated by the red chromophore, and an outer region that is dominated by fresh, high-albedo icy particles from the E-ring. Complicating the picture, how-ever, is the possible influence of interactions with magnetospheric particles, which have been shown to alter the color and albedo of the main moon system of Saturn (13, 14). It is unclear whether any volatiles other than water ice exist on the ring moons. The presence of molecules with higher volatility than water ice would in-dicate material originating in a colder region outside the saturnian system; for example, the discovery of CO2 ice on the irregular outer moon Phoebe suggested that it originated in the Kuiper Belt (15).

The last phase of *Cassini*'s mission began on November 30, 2016 and ended on September 15, 2017, with two distinct periods: the "Ring-grazing" (or F-ring) Orbits, when 20 close passes to the F-ring were accomplished, and the Proximal Orbits (the "Grand Finale"), when 23 dives between the planet and the main ring system were executed. During the Ring-grazing Orbits there were five "best-ever' flybys of Pan, Daphnis, Atlas, Pandora, and Epimetheus. Data were obtained by the four remote sensing instruments on *Cassini*: The Imaging Science Subsystem (ISS; 15); The Visual Infrared Mapping Spectrometer, with medium resolution spectra between 0.35 and 5.1 µm (VIMS; 16); The *Cassini* Infrared Spectrometer (CIRS; 17); The Ultraviolet Imaging Spectrometer (UVIS; 18); and *Cassini's* fields and particles experiments, two of which obtained simultaneous data that are described in this paper, the Cosmic Dust Analyzer (CDA; 19) and the Magnetosphere Imaging Instrument (MIMI; 20). In this paper we discuss the first results from the closest flybys of these moons, the details of which are summarized in Table 1. In addition to the "closest-ever" flyby of Epimetheus on January 30, 2017, a second flyby of this moon, which was also better than any previous event, occurred on February 21, 2017, with a closest approach of 8088 km. Valuable data on the dust and plasma environment in the vicinity of the small inner moons were also captured by the particles experiments during the subsequent Proximal Orbits.

[Table 1 here]

## Geology and morphology

Previous images of the ring moons showed distinctive equatorial ridges on Pan and Atlas (4,5) that were interpreted as likely formed by accretion of ring particles, whereas images of Daphnis were ambiguous as to the morphology of any near-equatorial ridge. The small satellites are all in synchronous rotation, tidally locked to the planet (6). Prometheus and Pandora's orbits straddle the F-ring, and although they exhibit different surface morphology, their densities are nearly identical (Table S1). The small (< 5 km mean radius) satellites Aegaeon, Methone, and Pallene that orbit in diffuse rings or ring arcs (21, 22) have smooth ellipsoidal shapes indicative of hydrostatic equilibrium (6). The co-orbital satellites, Epimetheus and Janus, by far the largest of the inner small moons, were found to have nearly identical mean densities (Table S1), also the highest among the inner small moons. Grooves had been observed on Epimetheus (23), and there were suggestions of discrete crater-filling sediments on both Janus and Epimetheus (6). Epimetheus was observed well enough to establish a ~7° forced wobble (libration) around a purely synchronous rotation (24). TableS1 summarizesthe shapes,volumes, and calculated mean densities of the small sat-ellites of Saturn based on the images taken during the flybys (26, 27). Epimetheus and Janus have densities substantially above 500 kg m–3;the lowest density (and highest uncertainty) is that of Daphnis, at 274 ± 142 kg m–3. Surface ac-celerations vary substantially across each object because of their irregular shapes and tidal ac-celerations (table S1).

*Main Ring moons and ridges*

The high resolution data make clear that the equatorial ridges on Pan and Atlas are distinct from what appears to be a more structurally competent "core" of each moon, and that ridges are different on all three main ring satellites. The fractional volumes of the ridges are Pan ~10%; Daphnis ~1%, and Atlas ~25%. Atlas's ridge is smooth at 76 m/pixel, with some elongate to irregular brighter albedo markings. It grades into a core with distinct ridge and groove topography (Fig. 1.), with a slightly polygonal equatorial profile previously known (6). Pan's ridge has distinct topographic margins with the core, with a somewhat polygonal equatorial shape, and it has some grooves, small ridges, and even some small impact craters. Meridian profiles across Pan's ridge vary considerably with longitude. Fig. 2 shows Pan in the best northern view, with calculated relative gravitational topography and surface slopes. Pan's ridge is not the result of material sliding toward areas made low by rotation and tides as are some ridges on small asteroids (27, 28) as slope directions are not latitudinally directed. The distinct boundary between ridge and core, the distinct surface morphology on each, and the large differences in relative heights along the ridge require the formation of this ridge to be unrelated to surface, gravity-driven processes. These observations are consistent with formation of the ridge by accretion of particles, the pattern being dictated by the relative orbital and rotational dynamics of the core and ring particles (5).

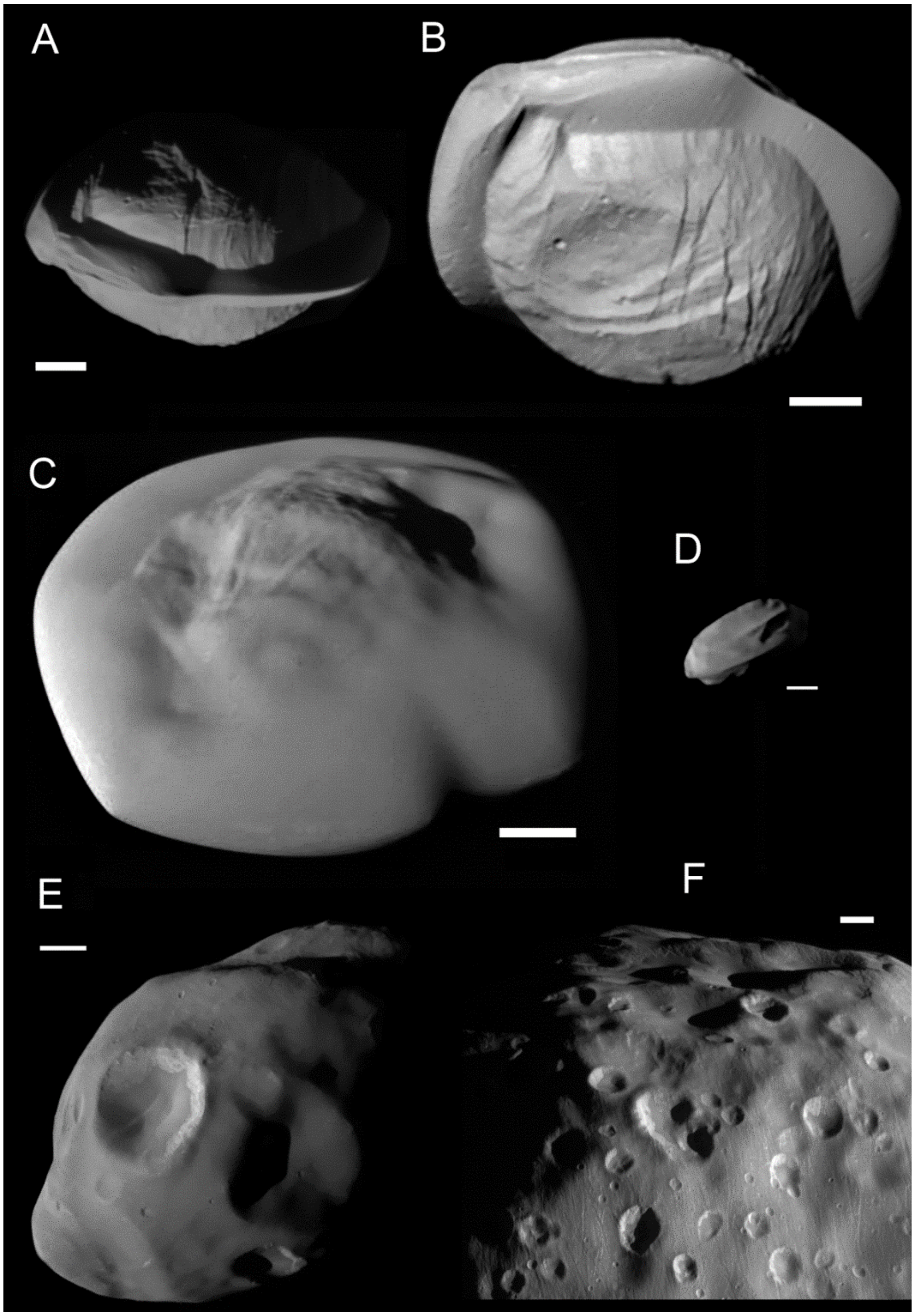


Fig 1. **Grayscale images of the ring moons obtained with ISS during the Cassini flybys. (A)** Pan, N1867606181, from 26ºS. Scale bar 5 km. Obtained at 182 m/pixel (m/p). **(B)** Pan, N186704669, from 39ºN; scale bar 5 km; 147 m/p. **(C)** Atlas, N1870699087, from 40ºN; scale 5 km; anti-Saturn point at lower left; 108 m/p. **(D)** Daphnis, N1863267232, from 14ºN; anti-Saturn point to left; scale 2 km; 170 m/p. **(E)** Pandora N1860790629 Scale bar 10 km. Sub spacecraft point is 35ºN,98ºW; north pole is close to two small craters above large, bright-walled

crater; 240 m/p. **(F)** Epimetheus. N1866365809; Grooves and craters dominate the surface. Scale 5km; 99 m/p. (The N numbers are the image identifiers.)

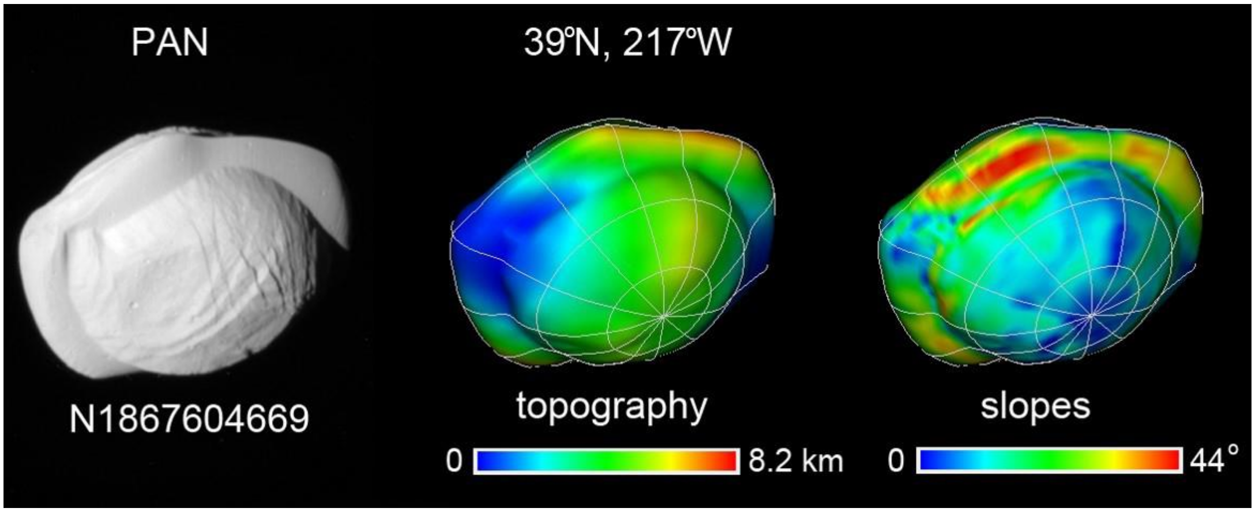


Fig. 2. **Relative topography and slopes on Pan.** Topography is relative potential energy at surface due to assumed homogeneous interior density, rotation, and tides, divided by an average surface acceleration. Slopes are angles between surface normals and net acceleration vectors (negative).

The nominal mean densities of all three main ring moons give calculated surface accelerations near zero at the sub- and anti-Saturn points. The remainder of all the surfaces has inward directed net accelerations. These results suggest the ends may be limited by their ability to accrete materials, but there is much to be explored in the dynamics of accreting and/or modifying these ridges.

The surfaces of the ring moons may be crudely divided into three units on the basis of morphology, geography, and texture of surface visible at the available resolutions (Fig. 3). The equatorial ridges generally have smoother surfaces than do the "cores."

The cores have more impact craters than do the ridges on Pan and Atlas which display a few sub-kilometer impact craters. Pan and Atlas' cores show lineated topography indicative of body structure. Pan has two distinct global sets of quasi-parallel faults, one of which is roughly concentric to the long axis and exhibits conspicuous scarps and terracing from likely equatorward displacements. Axial symmetry of this system suggests that tidal forces were involved in its development. The second system trend is oblique to the first, and is well expressed in both north and south hemispheres (Figs.1, 3). By contrast, Atlas' core exhibits patterns of elongated ridge and groove topography that do not have fault scarp morphology, and appear covered by at least tens of m of loose regolith.

Pan's equatorial ridge is thickest north-south at longitudes of approximately 220°, 310°, 135°, and 50° W, yet its radial extent peaks at longitudes of 5°, 55°, 100°, 180°, 235°, and 310°. It supports grooves and small craters: their presence suggests some cohesion in this extreme low-g environment. Atlas's equatorial profile is also somewhat polygonal, but not as pronounced as Pan's.

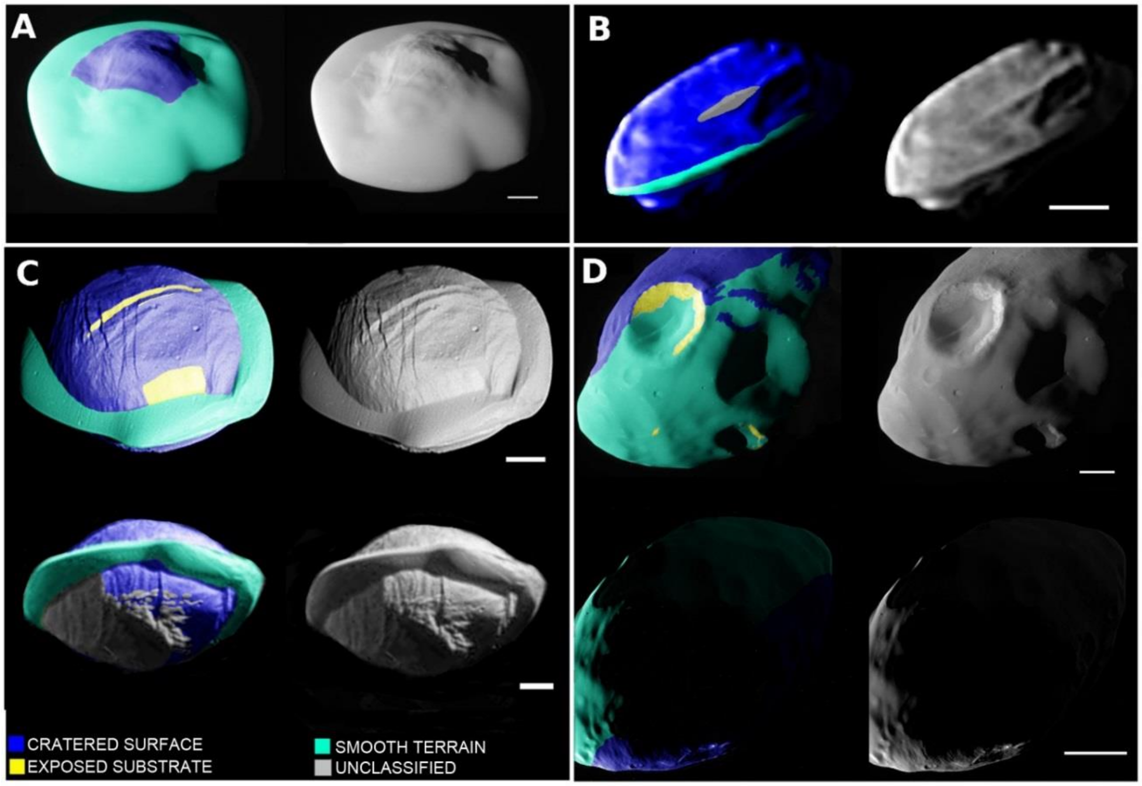


Fig. 3. **Distribution of geological units on Pan, Atlas, Daphins, and Pandora** **(A)** Atlas, scale bar 5 km. Obtained at 94m/pixel (m/p). **(B)** Daphnis, scale bar 2km; 167 m/p. **(C)** Pan scale bars 5 km; 144 m/p (top) and 279 m/p (bottom). **(D)** Pandora (top scalebar, 10km, bottom, 20 km); 137 m/p (top), 200 m/p (bottom). Cratered surface: heavy cratering, relatively crisp surface relief, and regolith typical of other small bodies in the Saturnian system. Smooth terrain: distinctly smooth compared to typical small body cratered surfaces; some is material collected in crater floors. Exposed substrate: relatively bright with lineations more typical of rigid materials than of loose regolith. Unclassified materials are those for which insufficient data are available to resolve ambiguities between terrain types.

The classification of some material units on Pan's southern hemisphere is ambiguous, in part because more of these regions are illuminated only by Saturnshine. These currently unclassified units in Fig. 3 include knobby streaks of hummocky material that trend approximately parallel to the equator and hummocky deposits that outline a curvilinear depression on the Saturn-facing side.

The best-available spatial resolution of Daphnis imaging is poorer, 170 m/pixel vs. that of Pan (147 m/pixel) and Atlas (76 m/pixel), and Daphnis is only about a quarter the dimensions of the other ring moons. As a result, it is not clear that its near-equatorial ridge is any smoother or otherwise different from the rest of the satellite surface. The equatorial ridge extends at least from 75°W to 185°W. An additional ridge at 22°N runs from ~ 60°W to 120°W. Both ridges are 300-400m north-south, and perhaps radially 300 m in extent. The core has an elongated (2.5 km) depression that is roughly aligned east-west.

*F-ring moons*

Prometheus and Pandora orbit inside and outside the F-ring. The higher resolution achieved on the Pandora flyby provided better coverage of the geography of grooves and debris on the surface of this "shepherding" moon (Fig. 1). Although many of the grooves form a familiar pattern concentric to the major axis of the body, there is a slight offset of the pattern especially noticeable on the sub-Saturn side, which reflects the orientations mapped earlier (21).

ISS closeup images of Pandora revealed that part of the leading hemisphere seen in Fig. 1 is smooth in comparison to other regions of Pandora (Figs. 1,3). The smooth deposits are most continuous near the equator but they become patchy at high latitudes where they appear to be too thin to mute the coarse surface relief along protruding crater rims. The smooth deposits extend approximately ±60° in latitude, most like the broad extent of the ridge on Atlas. This arrangement might indicate the accretion of material as on the main ring moons. If so, its efficacy on Pandora is at least two orders of magnitude smaller than on Pan and Atlas, and much broader latitudinally. However, variations in resolution, illumination, and viewing geometry make mapping of textural variations on Pandora ambiguous.

*Co-orbitals moons*

The highest resolution images of the flybys were of Epimetheus, the smaller of the co-orbitals, reaching scales of 36 and 49 m/pixel. These data greatly enhanced mapping of grooves and sediment coverings, both seen in lower resolution data (23). The grooves are global in occurrence, and are largely the typical beaded to straight, elongated depressions that appear to be features formed in loose regolith. There are some exposures of brighter material apparently devoid of regolith cover (Fig. 1F) that also show elongate lineations, generally slight depressions. These align with the grooves nearby that appear to be regolith features, and largely align with the regolith groove global patterns. This association appears to support a relation of at least some regolith grooves to fractures or other structures in a more rigid underlying "bedrock," although the variety of groove morphologies on many objects suggest grooves may have a multiplicity of origins (29, 30, 23, 31). The highest resolution images also show exposures of crisscrossing linear ridges and other lineations. If representative of the interior, these features suggest structure and history far different from simple accumulation of a "rubble pile."

*Colors of the Small Ring Satellites and Pandora*

The whole-disk colors of the ring satellites as measured in ISS broadband filters (32) follow similar trends with distance from Saturn as those found by the VIMS instrument (7-10). The ISS Narrow

Angle Camera (NAC) uses paired broadband filters. The CL1:UV3 pair (341 nm) and CL1:IR3 pair (930 nm) span the spectral range of the camera, and IR3/UV3 ratios can represent the ratio of observed brightness values in each of the broadband filters (cf. 6). For reference, Enceladus, the presumed source of ice particles that mute colors on other satellites, has an effectively neutral IR3/UV3 ratio of $1.03 \pm 0.02$ (33).

Pan, Daphnis, and Atlas are expected to show effects of material deposited from the rings. Closest to Saturn, Pan's average IR3/UV3 ratio of $2.5 \pm 0.2$ is red but significantly smaller than the value of $3.3 \pm 0.2$ of the adjacent A-ring (i.e., it is less red than the rings). Farther out, the A-ring IR3/UV3 ratio decreases from $2.7 \pm 0.2$ on the inside of the Keeler gap (which contains Daphnis) to $2.2 \pm 0.3$ on the outside. The mean value is not statistically different from the value of $2.3 \pm 0.3$ of Daphnis itself. The equatorial ridges on the ring satellites may be very old (4) but the colors most likely reflect a patina of material deposited from geologically recent and ongoing processes. Atlas, which falls just outside the A-ring has an IR3/UV3 ratio $2.4 \pm 0.1$. Pandora, with its value of $1.9 \pm 0.1$, is close to the F-ring farther from Saturn. It lacks an equatorial ridge but possesses smooth deposits which on the leading side extend from the equator to mid-latitudes.

Among the terrains shown in Fig. 3 color differences can be identified from the high-resolution images on all but Daphnis, for which the CL1:UV3 images were badly blurred by spacecraft motion. The IR3/UV3 ratio for cratered materials on Pan is about 19% higher than for its equatorial ridge and is most like the average global value. Similarly, the ratio for cratered materials on Atlas is about 16% higher than for its ridge, but in this case, the global average value not surprisingly most closely matches that for Atlas' larger equatorial ridge. For Pandora, the cratered materials have a IR3/UV3 ratio that is 15% *lower* than for the smooth materials towards the equator. The global average ratio is in between that for the cratered material and the smooth deposits. Exposed substrate is visible as a scarp on Pan and a bright exposed crater wall on Pandora. On Pan, the IR3/UV3 ratio of exposed substrate is intermediate between the ridge materials and crater materials. However, on Pandora, the corresponding ratio for the exposed crater wall is not statistically distinguishable from that of the cratered material.

## Composition

Most of the compositional information on the surfaces of Saturn's moons has been obtained by VIMS (16). Prior to the close flybys of the ring moons, some spectra were gathered by VIMS and rudimentary compositional information was obtained (7-10). Water ice was the only volatile identified, but the moons' visible colors varied, especially in the 0.35-0.55 μm spectral region, which suggested contamination by a reddish chromophore that perhaps came from the ring system itself. The identity and source of this chromophore was one of the main questions still remaining at the final stages of the *Cassini* mission. (This coloring agent is distinct from the low-albedo red material from the Phoebe ring that is deposited on the leading hemisphere of Iapetus and on Hyperion (7, 8).)

The close flybys of the embedded moons Daphnis and Pan enabled the acquisition of spectra of these moons for the first time, although only an IR spectrum (1.0-5.0 μm) for Daphnis was successfully obtained. These new data provide a key test for the origin of the red chromophore in the inner Saturnian system. These observations also provide rudimentary information on spatial variations in composition on the moon's surfaces, although the resolution is only about 1-2% (depending on the instrument mode) of ISS's (Supplementary materials)

Fig. 4 shows the spectrum of each moon from 0.35-5.0 µm (1-5.0 µm for Daphnis). The only spectral absorption bands detectable in these images are the water ice bands at 1.25, 1.6, 2.0 and 3.0 µm. No other volatiles are detectable, including $CO_2$, although its prime absorption band in this spectral region is at 4.26 µm, which is in the noisy region of the spectrum beyond about 3.5 µm. One interesting feature of these spectra is the relatively large depth of the absorption band for crystalline water ice at 1.65 µm. This spectral band is sensitive to radiation damage (34); its unusual depth implies a lack of this type of damage in the ring environment, which is expected given the dearth of high-energy particles in the rings (see the section on particle observations). Water ice spectral bands are also sensitive to grain size, with deeper bands signifying larger sizes (35). A larger particle size could signify larger regolith grains in the main ring system than in the E-ring, or it could simply be due to gravitational escape of the smaller particles, some of which could be formed by continual impacts.

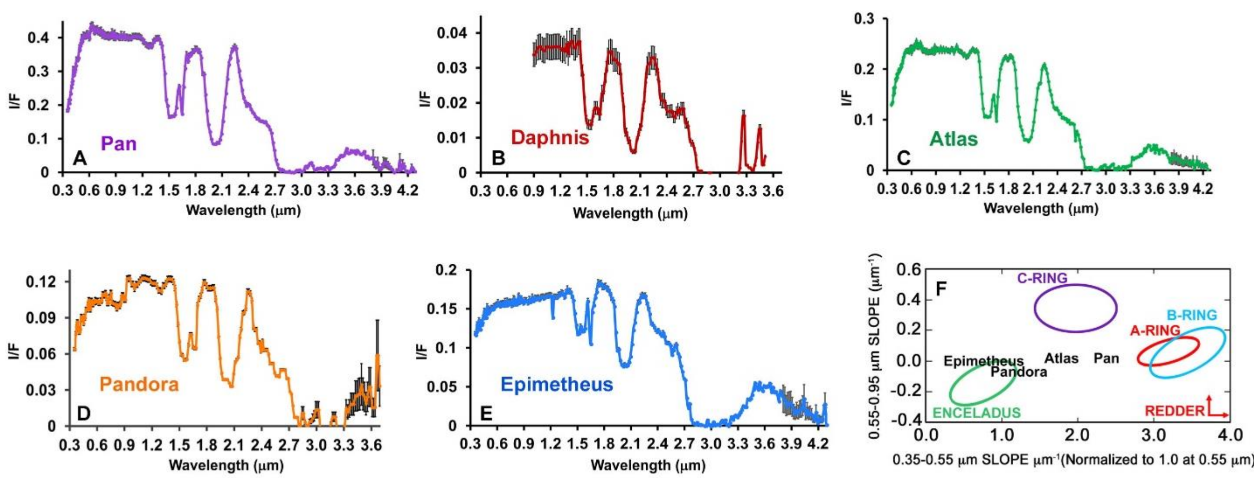


Fig. 4. VIMS **Spectra and colors of the five moons and the A- to C-rings (A to E) Spectra of Pan (A), Daphins (B), Atlas (C), Pandora (D), and Epimetheus (E). Noisy data at the long wavelengths are shown. I/F is the reflected intensity compared with the incident solar flux. (F) Color-color plot of Saturn's main ring system and Enceladus (7,8) compared with Epimetheus, Atlas, Pandora, and Pan.**

The VIMS visible colors show good agreement with those derived by ISS with equivalent VIMS numbers of the IR3/UV3 ratios of 2.7 ± 0.3 for Pan; 2.2 ± 0.2 for Atlas, 1.7 ± 0.2 for Pandora, and 1.5 ± 0.1 for Epimetheus (the VIMS spectrum extends to only 0.35 µm: this value was used for UV3 and the error bars adjusted accordingly). The moons embedded in the rings show important spectral differences with the surrounding rings; in general they are less red (Fig. 4F). The VIMS ratio image of Atlas shows uniformity between the main body and its equatorial ridge, at least in water ice abundance, which implies accumulation of particles away from the equator to provide a globally homogeneous surface. Color differences below the spatial resolution of VIMS may exist, as detected by ISS in the visible.

The most striking difference among these new spectra is the difference in color measured by the slope between 0.35 and 0.55 µm. The new spectrum of Pan is extraordinarily red compared to other Saturnian moons. Atlas, the shepherd moon just outside the A-ring, is also red but less so, and Pandora, which is associated with the F-ring, even less. The color of Epimetheus is more like that of the medium-sized moons (7-9). Thus, there is a gradient in color with distance from Saturn's ring system, with the embedded Pan being the most red. This view is clear in Figure 4A-E, where the slope of the visible spectrum increases sharply as the distance to Saturn increases, and it is quantified in Fig. 4F, which shows the visible colors derived from the recent close flybys with the colors of the main ring system of Saturn (8). These results imply the red chromophore comes from the rings themselves. However, the differences in color between the moons and their adjacent rings – the small moons are consistently bluer than their surrounding rings - could be due to another contaminant: particles of almost pure water ice from the E-ring. This ring is a diffuse torus that is fed from the plume of Enceladus. The particles have a wide range of orbital elements and predominately impact the leading sides of the main moons (or the trailing side of Mimas) to alter their albedo and color (36-38). The ring moons' leading hemispheres would tend to be "painted" by fresh grains and accrete more water ice than the surrounding ring particles.

The depth of the water ice band at 2.0 µm compared to the continuum at 1.8 µm (1.8/2.0 µm) is 5.2±0.1 +0.1 for Pan, 5.0±0.2 for Daphnis; 4.4±0.1for Atlas, 3.4±0.1 for Pandora, and 2.4±0.1 for Epimetheus. The band-depths increase closer to Saturn, most likely due to the increasing particle sizes (35). This view is consistent with the moons embedded in the ring (Pan and Daphnis) being coated with main ring particles rather than with smaller particles from the E-ring. (The absorption band at 1.6 µm shows a similar but weaker trend).

Interactions between moons and magnetospheric particles can also alter the moons' colors and albedos (12, 13). However, results from the fields and particles experiments in the vicinity of these moons showed a dearth of high energy particles with the expectation that these alterations would be slight (see below).

## Ultraviolet and Thermal Infrared Observations of the Moons

During the Ring-grazing Orbits the spacecraft was in a radiation and dust environment that resulted in high background levels for UVIS. One successful detection was made of Epimetheus during the encounter on Feb 21, 2017. Even on that flyby, the signal is only above the background for the longest FUV wavelengths, ~0.170-0.19 µm. However, this single UV measurement of reflectance places some constraints on surface composition and exogenic effects on Epimetheus. At 72° solar phase angle (the angle between the spacecraft, Epimetheus, and the Sun), the derived normal reflectance averaged between 0.17-0.19 µm is 0.09±0.02. For comparison, this number is roughly 1.5-2 times lower than the reflectance measured at Tethys under similar viewing geometry; however, Tethys has a significantly higher visible geometric albedo (~1.2 compared to ~0.73 for Epimetheus (36)), which indicates that Epimetheus may have a roughly uniformly lower reflectance than Tethys in the UV-visible range. The UV-visible spectral slope and albedo are strongly driven by exogenic effects, since this spectral range senses the uppermost layer of the regolith affected by processes including radiolysis and E-ring grain bombardment. The UVIS result combined with the knowledge of the visible albedo may suggest that Epimetheus is not as affected by the brightening effects of the E-ring grains as Tethys is (36), or that there is some other darkening agent or process important at Epimetheus's location. Thus, the UV-visible albedo of Epimetheus may simply reflect the relative importance of the alteration by the reddish lower-albedo chromophore and the icy E-ring particles at this moon's distance.

CIRS made positive detections of two moons: Epimetheus and Atlas (supplemental materials). The results are given in Fig. 5, which shows the temperature that has a blackbody emission curve best able to fit the observed radiance over all wavelengths. Both Epimetheus and Atlas are clearly visible above the background dark sky. The mean surface temperature observed on Epimetheus is 90.1±2.7 K, and 82.4±4.7 K on Atlas.

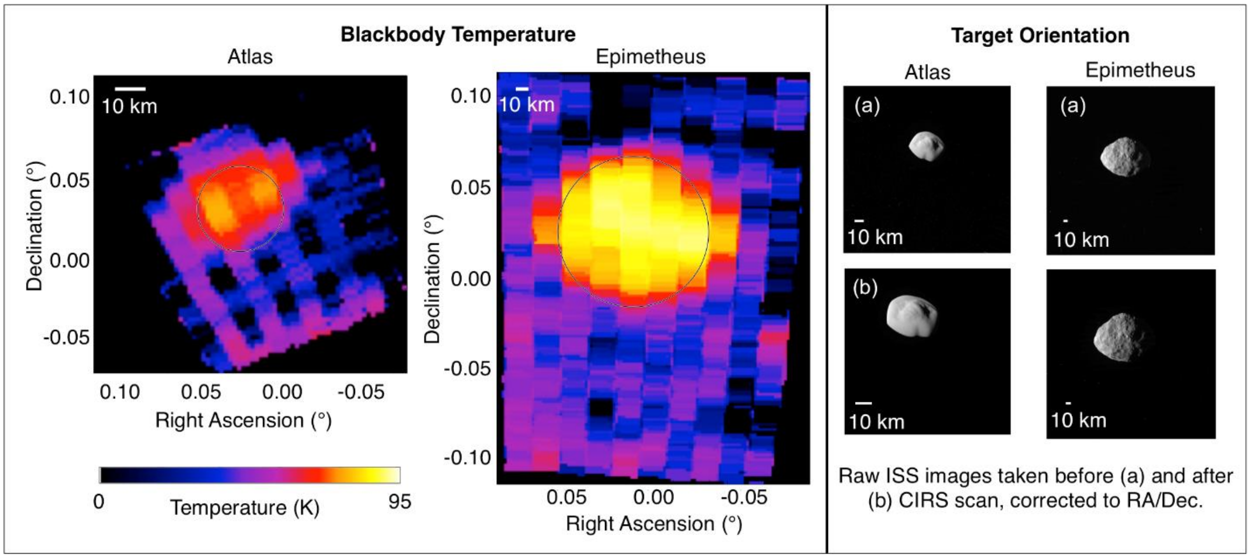


Fig. 5. CIRS and ISS observations of Atlas and Epimetheus. Left: The blackbody temperature of the two targets, as determined by fitting a blackbody curve to the full CIRS radiance spectrum at each location. The results are shown in Right Ascension/Declination space, which has been corrected so the center of the target lies at 0°/0°. Right: Raw ISS observations of both targets taken before and after the CIRS scan (supplemental materials).

## Particle Observations

Throughout the Ring-grazing Orbits, the Particle and Fields experiments obtained unprecedented coverage of Saturn's plasma and dust environment, including detailed measurements of the region around the small inner moons. First results from the analysis of this data provide a basic understanding of whether the surfaces of these bodies are altered by the dusty plasma, and what effects the moons have on the environment, such as forming tori or cavities.

In the course of the Ring-grazing Orbits, *Cassini* passed close to the orbits of the co-orbital moons Janus and Epimetheus. During 11 of the 20 ring plane crossings, the High Rate Detector (HRD) of CDA detected in total about 2,000 dust grains with radii larger than 0.8 μm. While the vertically integrated number density of grains smaller than 1.6 μm does not depend on the radial distance to

Saturn, the density of bigger grains drops by about 50% over a radial distance of approximately 3500 km (Fig. 6). The larger particles are less susceptible to non-gravitational forces and, therefore, particles ejected from the moons stay closer to their parent bodies and form a more confined ring (39). The fit of a Gaussian distribution including the dust background from the F- and G-rings to the HRD data constrains the radial width of the ring (FWHM) to about 4,300 km leading to a total number of ring particles larger than 1.6 μm of $2 \cdot 10^{19}$.

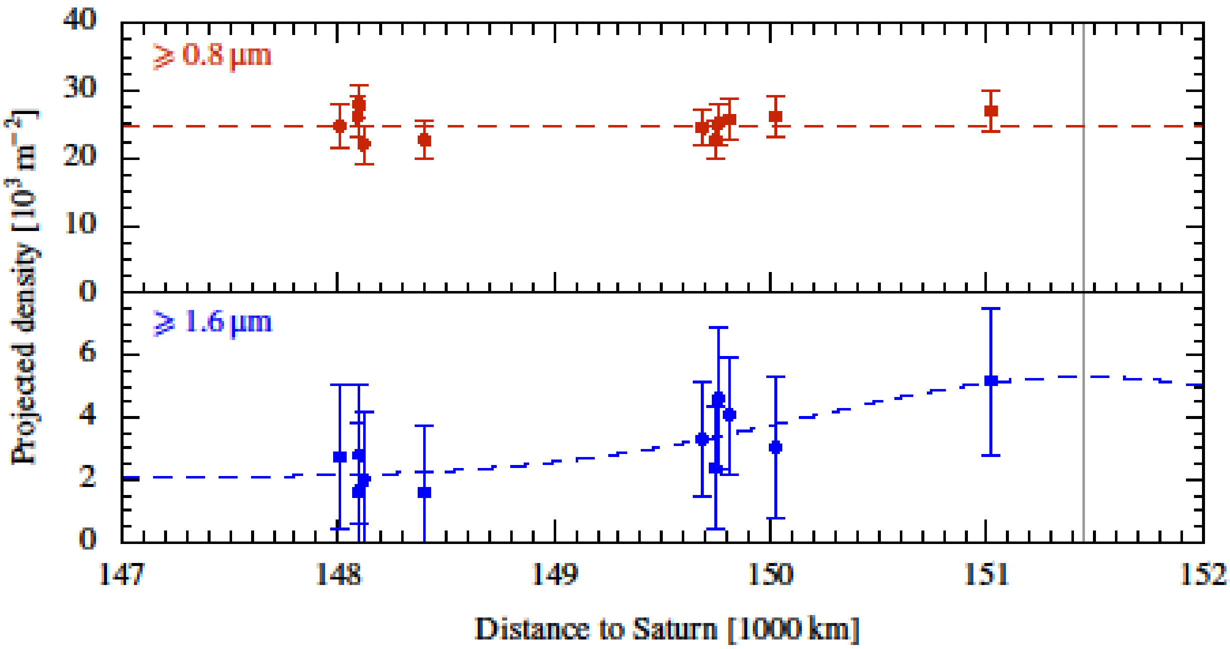


Fig. 6. **Radial density distribution obtained from *Cassini* CDA-HRD dust measurements**. While the density of the > 0.8μm sized particles can be well-fitted by a constant profile (red dashed line), the density of the ≥ 1.6 μm sized particles decreases inward from the orbit of Janus and Epimetheus. The dust distribution of the larger particles is modeled by a Gaussian distribution (blue dashed line) with a maximum at the mean radial position of Janus and Epimetheus (vertical gray line) including a constant background density.

Many dust rings are formed by ejecta from high-velocity impacts of interplanetary micrometeoroids eroding the surfaces of satellites without atmospheres. The measured particle number in the Janus-Epimetheus ring constrains the poorly known parameters of the impact-ejection dust creation model (40,41) at Saturn, although more recent work by CDA indicates a higher flux. Using an unfocussed flux of $> 2.7 \cdot 10^{-16}$ kg $m^{-2} s^{-1}$ with an impact speed of 4.3 km $s^{-1}$ (42), the dust production rate from both moons is about 0.91 kg $s^{-1}$. (0.64 kg $s^{-1}$ from Janus and 0.27 kg $s^{-1}$ from Epimetheus). This corresponds to $9.8 \cdot 10^{11}$ particles larger than 1.6 μm per second ($6.9 \cdot 10^{11}$ $s^{-1}$ from Janus and $2.9 \cdot 10^{11}$ $s^{-1}$ from Epimetheus) assuming a cumulative power law size distribution $\propto s^{-\alpha}$ with $\alpha = 2.4$ and a maximal ejecta mass of $1 \cdot 10^{-8}$ kg consistent with observations of impact-generated dust clouds around the Galilean moons (43, 40).

To explain the measured number of ring particles, this comparably high production rate requires a shallow slope of the cumulative ejecta velocity distribution $\propto v^{-\gamma}$ ($\gamma$=1), and a higher kinetic energy dissipation than predicted by laboratory experiments (kinetic energy ratio of ejecta to impactor is 5%). This points to a highly dissipative and porous (snow or regolith) surface. With this result, we find that most impact-ejecta are gravitationally bound to the moons and fall back to their surface, while only about 6% of them escape to the ring. Numerical simulations reveal that most of the ring particles are recaptured by Janus and Epimetheus after an average lifetime of 60 years resulting in an estimate of $1 \cdot 10^{20}$ ring particles larger than 1.6 μm. This is, considering the large uncertainties of the impact-ejection model, in fair agreement with the observed value of $2 \cdot 10^{19}$ (supplementary material)

Additionally, the CDA Chemical Analyzer (8) has recorded spectra of submicrometer-sized dust particles (0.1µm - 0.4µm). The compositional analysis of these spectra shows mostly ice grains but also a few percent pure silicate grains or ice-silicate mixtures. The source of the icy particles could either be the inner edge of the E-ring or surface ejecta of the nearby small ice moons. Because silicate-rich grains of this size have not been detected in the E-ring, these must originate from a different source, possibly the nearby moons Janus and Epimetheus or the F- and G-rings.

The Low Energy Magnetospheric Measurements System (LEMMS) of the MIMI energetic charged particle detector made the first comprehensive survey of the planet's radiation belts inward of Saturn's G-ring and monitored the environment of the five small moons. LEMMS measures energetic electrons and ions from 18 and 27 keV respectively, and well into the MeV energy range. The region inward of Saturn's G-ring has been sampled in the past on several occasions with Pioneer 11 and *Cassini* (44-46). It contains the location where both proton and electron radiation belts have their highest intensities, between the G-ring and Janus and Epimetheus's orbits. Inward of that maximum intensities drop gradually up to the outer edge of Saturn's A-ring which absorbs all energetic particles. Superimposed on the radial profile of radiation belt fluxes are localized dropouts originating from Saturn's moons and rings (47). While several of these features can be attributed to specific moons, like Janus and Epimetheus (48), any influences by Pandora, Prometheus and Atlas (orbiting within the radiation belt boundaries) are less clear. These moons orbit close to Saturn's A and F-rings and separating the different contributions was not possible until now due to the low statistical significance of any past observations. Understanding how effectively these moons sweep-out particle radiation is also important for describing the space weathering environment to which their surfaces are exposed to.

Fig. 7A shows count-rates of >12 and >25 MeV protons as a function of L-shell (L), averaged from all the Proximal Orbits. The L-shell is defined as the distance from Saturn that a field line intersects the magnetic equator and is given in multiples of the planet's radius (1 Rs = 60268 km). The L-shell here describes the equatorial footpoint of Cassini's trajectory mapped along Saturn's magnetic field, normalized to one planetary radius of 60268 km. A third-order multipole model for Saturn's internal magnetic field was used to derive its value (47). The plot shows the well-established sectorization of the MeV proton radiation belts, due to the moons and rings that absorb any protons diffusing across their orbits (50,51). Among these different sectors, the least characterized is the one we mark here as the "Minor Belt", centered at approximately L=2.29 and sampled only twice before the Proximal Orbits. The belt gap outward of the Minor Belt is centered near the F-ring (L~2.32) and the increased sampling of that region has verified that those gap's boundaries coincide with the L-shells of Prometheus and Pandora (Fig. 7A - inset). Pandora and Prometheus are therefore absorbing protons at a rate that is strong enough to counter the diffusive influx of protons from the surrounding belt sectors. Effectively, the two moons and the F-ring form an extended obstacle to proton radiation. The net result is that the weathering of Pandora's and Prometheus's surfaces by energetic protons is negligible since they orbit within the proton radiation gaps they create. Atlas's effects could not be distinguished from those of the A-ring, but that moon is also exposed to very low proton fluxes. Overall, it is now established that almost all of Saturn's inner moons (except Dione, Rhea or minor moons like Anthe or Pallene) orbit in energetic ion free environments (52-54), a striking difference from that of the Jovian satellites whose surface chemistry and exospheric properties are strongly affected by irradiation from high fluxes of keV and MeV protons, oxygen and sulfur (55,56).

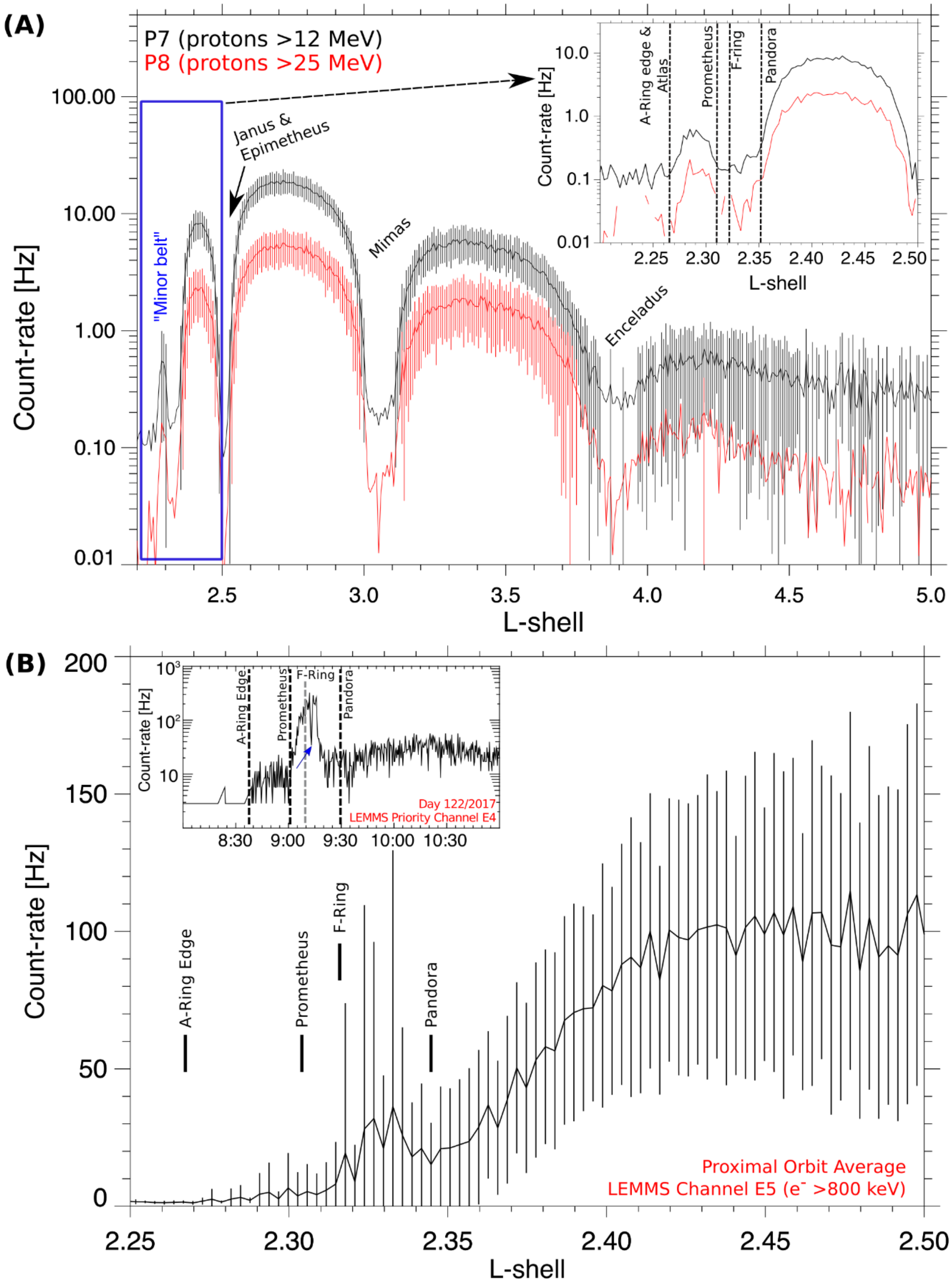
(A)
P7 (protons >12 MeV)
P8 (protons >25 MeV)
"Minor belt"
Janus & Epimetheus
Mimas
Enceladus
Count-rate [Hz]
L-shell
A-Ring edge & Atlas
Prometheus
F-ring
Pandora
(B)
A-Ring Edge
Prometheus
F-Ring
Pandora
Day 122/2017
LEMMS Priority Channel E4
Proximal Orbit Average
LEMMS Channel E5 (e⁻ >800 keV)
Count-rate [Hz]
L-shell

Fig. 7A**. Proximal orbit averaged count-rates of MIMI/LEMMS proton channels P7 and P8 (above 12 and 25 MeV respectively) as a function of L-shell, together with the 1-$\sigma$ error bars.** Absence of error bars indicates an error larger than the corresponding mean value. The orbits of several of Saturn's large icy moons are also marked. The inset zooms into the region of the Minor Belt, highlighting the absorbing effects of Atlas, Pandora, Prometheus and the A- and F-rings. Fig. 7B. **Proximal Orbit averaged count-rates of MIMI/LEMMS electron channel E5 (>800 keV) as a function of L-shell.** Overplotted are the 1-$\sigma$ error bars at each L-shell bin. The locations of various moons and rings are also marked, as in Panel A. The inset shows time series of high time resolution observations (1 sample per 0.3125 sec) from LEMMS channel E4, which has a similar response to E5. The data were obtained from the second proximal orbit, on May 2, 2017. A blue arrow marks an electron microsignature within one of the MeV electron "spikes" seen consistently during *Cassini*'s outbound crossings near the L-shell of the A-ring's outer edge.

Fig. 7B shows Proximal Orbit averages of electron count-rates from LEMMS channel E5 (>0.8 MeV) as a function of L-shell. Electron radiation levels are more variable than those of protons, as the sizeable error bars indicate, since moons and rings are not effective in sweeping out electrons from their orbits (47,52,57). Inside L=2.4 (inwards of the Janus and Epimetheus orbits) electron rates start to experience a shallow drop towards the outer edge of the A-ring (L=2.27). This drop is interrupted by an unexpected enhancement of the mean electron rates, near the L-shells of the F-ring, Pandora and Prometheus. The statistical 1-$\sigma$ error bars in that location span more than two orders of magnitude in amplitude, indicating also much higher variability than in the surrounding regions. A survey of electron measurements from each Proximal Orbit reveals that this large scatter is attributed to spiky enhancements of MeV electron fluxes observed in all the outbound crossings outwards of the A-ring's edge and between L=2.31 and L=2.35. The radial extent of an individual spike is less than 1800 km along the equatorial plane, and the electron intensity within them can be enhanced by as much as a factor of 300 compared their surroundings. The inset of Fig. 7B shows one such resolved spike, captured by the high time resolution measurements of LEMMS Priority channel E4 (0.8-4.2 MeV) on May 2, 2017. Since most measurements in the inbound portion of Cassini's orbit showed no evidence of similar spikes in the same L-shell range, we deduce that these features are usually fixed few hours after local noon, and their longitudinal extent ranges between 22° and 37° starting from a magnetospheric local time of 14:50 and in the clockwise direction. The longitudinal extend cannot be constrained in the anticlockwise direction. Most of these enhancements were seen around the L-shells of the F-ring, Prometheus and Pandora. This unexpected electron belt component is therefore limited in local-time range. As a result, energetic electron bombardment of the three moons is variable in intensity, episodic and will occur only for a fraction of their orbit around Saturn. Material interaction signatures of energetic electrons are seen as localized depletions (microsignatures) within the electron spikes. These may have come from Atlas, Prometheus, Pandora or F-ring clumps (58); an example is shown with a blue arrow in the Inset of Fig. 7B and could have formed only after the electron enhancement developed. The age of such microsignatures can therefore set limits to the lifetime of these transient electron structures and inform theories of their formation.

Finally, a first survey of the LEMMS measurements from times that *Cassini* was magnetically connected to Saturn's main rings shows no discernible signal of trapped electron or proton radiation above the detection limit of the instrument at the orbits of the Keeler and Encke gaps, where Daphnis and Pan are orbiting.

## Summary and Conclusions

The low densities of the small moons of Saturn, which were refined by these close flybys, are still consistent with a multi-stage formation scenario involving accretion of ring material (4,5). The new data on the moons embedded in the A-ring show that the color of these moons becomes more similar to the rings the closer they are to Saturn. This result suggests there is an ongoing accretion of a reddish chromophore that may be a mixture of organics and iron, onto the surfaces of the moons. The difference in color between the moons and their adjacent ring may be explained by the accretion of bright, icy particles or, more likely, water vapor from the E-ring. In essence each moon's surface is subjected to a balance between these two ongoing processes, with their distance from Saturn and Enceladus determining the final result, as illustrated in Fig. 4F. The detection of abundant ice grains by CDA supports this view. The bluer core of Atlas is also explained by the accretion of E-ring particles, which have a wider range of inclinations than main ring particles. If the ring moons are made out of the same material as the rings, they would of course have been the same color, and the color gradient may come *solely* from contamination by the E-ring.

The finding by MIMI of a dearth of high-energy ions also lessens the competing alteration processes caused by the bombardment of magnetospheric particles. The strong crystalline water ice band at 1.65 µm also suggests the lack of importance of these processes. This "low energy" environment also renders comparisons with the identity of the red chromophore on the trailing hemispheres of main moons of Saturn, especially Dione and Rhea, problematical, as they dwell in a region where alterations by ions is significant and would tend to darken and redden the surfaces (57). Finally, the possible contamination of Saturn's rings by bright icy particles or water vapor qualifies the argument that the observed brightness of the rings bespeaks a recent formation (58).

The moons record a complex geologic history with groove formation caused by tidal stresses and accretion of ring particles. The CDA finding of a porous surface further supports substantial accretion. Although the topography and surface slopes strongly suggest the equatorial ridges of Pan and Atlas are accreted from the rings and are not formed by normal surface transport, the variety of forms of ridges on these objects, and the minimal ridges on Daphnis, show that much remains to be understood about their formation and relation to the main rings. The high resolution images strongly suggest exposures of a solid substrate distinct from the mobile regolith that frequently covers essentially all of many small Solar System objects. These exposures may eventually help reveal systematic trends of both solid body history and structures for the whole of the Saturn satellite system.

## Acknowledgements

The authors are grateful to the Cassini project engineers and staff for their dedicated service that led to the success of the final stages of the mission. Funding: This paper was funded by the Cassini Project. Part of this research was carried out at the Jet Propulsion Laboratory, California Institute of Technology, under contract to NASA. Also supported by Deutsches Zentrum für Luft- und Raumfahrt grants OH 1401 and 1503 and by Deutsche Forschungsgemeinschaft (DFG) grants Ho5720/1-1 and OH 1401 (M.Se., R.S., H.H., M.Sa., F.S., T.A., S.K., N.Kh., G.M.-K., F.P., and J.Si.), 50OH1501 (J.Si., G.M.-K., and T.A.), and 50OH1503 (T.D. and H.R.); the Italian Space Agency (G.F. and M.C.); and DFG projects PO 1015/2-1, /3-1, /4-1 and ERC Consolidator Grant 724908-Habitat OASIS (N.Kh. and F.P.).

**References**

Tiscareno, E. Turtle, A. R. Vasavada, J. Veverka, R. Wagner, R. West, *Cassini* imaging science: Initial results on Saturn's rings and small satellites. *Science* **307**, 1237-1242 (2005).

2. M. R. Showalter, Visual detection of 1981S13, Saturn's eighteenth satellite, and its role in the Encke gap. *Nature* **351**, 709-713 (1991).

3. B. A. Smith, L. Soderblom, R. F. Beebe, J. M. Boyce, G. Briggs, A. Bunker, S. A. Collins, C. Hansen, T. V. Johnson, J. L. Mitchell, R. J. Terrile, M. H. Carr, A. F. Cook, J. N. Cuzzi, J. B. Pollack, G. E. Danielson, A. P. Ingersoll, M. E. Davies, G. E. Hunt, H. Masursky, E. M. Shoemaker, D. Morrison, T. Owen, C. Sagan, J. Veverka, R. Strom, V. E. Suomi, Encounter with Saturn - Voyager 1 imaging science results. *Science* **212**, 163-191 (1981).

4. C. C. Porco, P. C. Thomas, J. W. Weiss, D. C. Richardson, Saturn’s small inner satellites: Clues to their origins. *Science* **318**, 1602 (2007).

5. S. Charnoz, A. Brahic, P. C. Thomas, C. C. Porco, The equatorial ridges of Pan and Atlas: Terminal accretionary ornaments? *Science* **318**, 1622-1624 (2007).

6. P. C. Thomas, J. A. Burns, M. Hedman, P. Helfenstein, S. Morrison, M. S. Tiscareno, J. Veverka, The inner small satellites of Saturn: A variety of worlds. *Icarus* **226**, 999-1019 (2013).

7. G. Filacchione, F. Capaccioni, R. N. Clark, J. N. Cuzzi, D. P. Cruikshank, A. Coradini, P. Cerroni, P. D. Nicholson, T. B. McCord, R. H. Brown, B. J. Buratti, F. Tosi, R. M. Nelson, R. Jaumann, K. Stephan, Saturn’s icy satellites investigated by *Cassini*-VIMS. II. Results at the end of nominal mission. *Icarus* **206**, 507-523 (2010).

8. G. Filacchione, F. Capaccioni, M. Ciarniello, R. N. Clark, J. N. Cuzzi, P. D. Nicholson, D. P. Cruikshank, M. M. Hedman, B. J. Buratti, J. I. Lunine, L. A. Soderblom, F. Tosi, P. Cerroni, R.

H. Brown, T. B. McCord, R. Jaumann, K. Stephan, K. H. Baines, E. Flamini, Saturn's icy satellites and rings investigated by *Cassini*-VIMS: III - Radial compositional variability. *Icarus* **220**, 1064-1096 (2012).

9. G. Filacchione, F. Capaccioni, R. N. Clark, P. D. Nicholson, D. P. Cruikshank, J. N. Cuzzi, J. I. Lunine, R. H. Brown, P. Cerroni, F. Tosi, M. Ciarniello, B. J. Buratti, M. M. Hedman, E. Flamini, The radial distribution of water ice and chromophores across Saturn's system. *Astrophys. J*. **766**, 76-80 (2013).

10. B. J. Buratti, J. M. Bauer, M. D. Hicks, J. A. Mosher, G. Filacchione, T. Momary, K. H. Baines, R. H. Brown, R. N. Clark, P. D. Nicholson, *Cassini* spectra and photometry 0.25-5.1 μm of the small inner satellites of Saturn. *Icarus* **206**, 524-536 (2010).

11. R. N. Clark, D. P. Cruikshank, R. Jaumann, R. H. Brown, K. Stephan, C. M. Dalle Ore, K. E. Livo, N. Pearson, J. M. Curchin, T. M. Hoefen, B. J. Buratti, G. Filacchione, The surface composition of Iapetus: Mapping results from *Cassini* VIMS. *Icarus* **218**, 831-860 (2012).

12. P. Schenk, D. P. Hamilton, R. E. Johnson, W. B. McKinnon, C. Paranicas, J. Schmidt, M. R. Showalter, Plasma, plumes and rings: Saturn system dynamics as recorded in global color patterns on its midsize icy satellites. *Icarus* **211**, 740-757 (2011).

13. A. R. Hendrix, G. Filacchione, C. Paranicas, P. Schenk, F. Scipioni, Icy Saturnian satellites: Disk-integrated UV-IR characteristics and links to exogenic processes. *Icarus* **300**, 103-114 (2018).

14. T . V. Johnson, J. I. Lunine, Saturn's moon Phoebe as a captured body from the outer Solar System. *Nature* **435**, 69-71 (2005).

15. C. C. Porco, R. A. West, S. Squyres, A. McEwen, P. Thomas, C. D. Murray, A. Del Genio, A. P. Ingersoll, T. V. Johnson, G. Neukum, J. Veverka, L. Dones, A. Brahic, J. A. Burns, V. Haemmerle, B. Knowles, D. Dawson, T. Roatsch, K. Beurle, W. Owen, *Cassini* maging science: Instrument characteristics and anticipated scientific investigations at Saturn. *Space Sci. Revs.* **115**, 363-497 (2004).

16. R. H. Brown, K. H. Baines, G. Bellucci, J.-P. Bibring, B. J. Buratti, F. Capaccioni, P. Cerroni, R. N. Clark, A. Coradini, D. P. Cruikshank, P. Drossart, V. Formisano, R. Jaumann, Y. Langevin, D. L. Matson, T. B. McCord, V. Mennella, E. Miller, R. M. Nelson, P. D. Nicholson, B. Sicardy, C. Sotin, The *Cassini* Visual and Infrared Mapping Spectrometer (VIMS) investigation. *Space Sci. Res.* **115**, 111-118 (2004).

17. F. M. Flasar, V. G. Kunde, M. M. Abbas, R. K. Achterberg, P. Ade, A. Barucci, B. Bézard, G. L. Bjoraker, J. C. Brasunas, S. Calcutt, R. Carlson, C. J. Césarsky, B. J. Conrath, A. Coradini, R. Courtin, A. Coustenis, S. Edberg, S. Edgington, C. Ferrari, T. Fouchet, D. Gautier, P. J. Gierasch, K. Grossman, P. Irwin, D. E. Jennings, E. Lellouch, A. A. Mamoutkine, A. Marten, J. P. Meyer, C. A. Nixon, G. S. Orton, T. C. Owen, J. C. Pearl, R. Prangé, F. Raulin, P. L. Read, P. N. Romani, R. E. Samuelson, M. E. Segura, M. R. Showalter, A. A. Simon-Miller, M. D. Smith, J. R. Spencer, L. J. Spilker, F. W. Taylor, Exploring the Saturn system in the thermal infrared: The composite infrared spectrometer. *Space Sci. Res.* **115**, 169-297 (2004).

18. L. W. Esposito, C. A. Barth, J. E. Colwell, G. M. Lawrence, W. E. McClintock, A. I. F. Stewart, H. U. Keller, A. Korth, H. Lauche, M. C. Festou, A. L. Lane, C. J. Hansen, J. N. Maki, R. A. West, H. Jahn, R. Reulke, K. Warlich, D. E. Shemansky, Y. L. Yung, The *Cassini* ultraviolet imaging spectrograph investigation. *Space Sci. Res.* **115** 299-361 (2004).

19. R. Srama, T. J. Ahrens, N. Altobelli, S. Auer, J. G. Bradley, M. Burton, V. V. Dikarev, T. Economou, H. Fechtig, M. Görlich, M. Grande, A. Graps, E. Grün, O. Havnes, S. Helfert, M. Horanyi, E. Igenbergs, E. K. Jessberger, T. V. Johnson, S. Kempf, A. V. Krivov, H. Krüger, A. Mocker-Ahlreep, G. Moragas-Klostermeyer, P. Lamy, M. Landgraf, D. Linkert, G. Linkert, F. Lura, J. A. M. McDonnell, D. Möhlmann, G. E. Morfill, M. Müller, M. Roy, G. Schäfer, G. Schlotzhauer, G. H. Schwehm, F. Spahn, M. Stübig, J. Svestka, V. Tschernjawski, A. J. Tuzzolino, R. Wäsch, H. A. Zook, The *Cassini* cosmic dust analyzer. *Space Sci. Res.* **114**, 465-518 (2004).

20. S. M. Krimigis, D. G. Mitchell, D. C. Hamilton, S. Livi, J. Dandouras, S. Jaskulek, T. P. Armstrong, J. D. Boldt, A. F. Cheng, G. Gloeckler, J. R. Hayes, K. C. Hsieh, W.-H. Ip, E. P. Keath, E. Kirsch, N. Krupp, L. J. Lanzerotti, R. Lundgren, B. H. Mauk, R. W. McEntire, E. C. Roelof, C. E. Schlemm, B. E. Tossman, B. Wilken, D. J. Williams, Magnetosphere IMaging Instrument (MIMI) on the *Cassini* mission to Saturn/Titan. *Space Sci. Res.* **114,** 233-329 (2004).

21. M. M. Hedman, C. D. Murray, N. J. Cooper, M. S. Tiscareno, K. Beurle, M. W. Evans, J. A. Burns, Three tenuous rings/arcs for three tiny moons. *Icarus* **199**, 378-386 (2009).

22. M. M. Hedman, N. J. Cooper, C. D. Murray, K. Beurle, M. W. Evans, M. S. Tiscareno, J. A. Burns, Aegaeon (Saturn LIII), a G-ring object. *Icarus* **207**, 433-446 (2010).

23. S. J. Morrison, P. C. Thomas, M. S. Tiscareno, J. A. Burns, J. Veverka, Grooves on small Saturnian satellites and other objects: Characteristics and significance. *Icarus* **204**, 262-270 (2009).

24. M. S. Tiscareno, P. C. Thomas, J. A. Burns, The rotation of Janus and Epimetheus. *Icarus* **204**, 254-261 (2009).

25. N. J. Cooper, S. Renner, C. D. Murray, M. W. Evans, Saturn's inner satellites: Orbits, masses, and the chaotic motion of Atlas from new *Cassini* imaging observations. *Astron. J.* **149**, 27-45 (2015).

26. J. W. Weiss, C. C. Porco, M. S. Tiscareno, Ring edge waves and the masses of nearby satellites. *Astron. J.* **138**, 272-286 (2009).

27. S. J. Ostro, J.-L. Margot, L. A. M. Benner, J. D. Giorgini, D. J. Scheeres, E. G. Fahnestock, S. B. Broschart, J. Bellerose, M. C. Nolan, C. Magri, P. Pravec, P. Scheirich, R. Rose, R. F. Jurgens, E. M. De Jong, S. Suzuki, Radar imaging of binary near-Earth asteroid (66391) 1999 KW4. *Science* **314**, 1276-1280 (2006).

28. A. W. Harris, E. G. Fahnestock, P. Pravec, On the shapes and spins of "rubble pile" asteroids. *Icarus* **199**, 310-318 (2009).

29. S. J. Weidenschilling, A possible origin for the grooves of PHOBOS. *Nature* **282**, 697 (1979).

30. D. L. Buczkowski, O. S. Barnouin-Jha, L. M. Prockter, 433 Eros lineaments: Global mapping and analysis. *Icarus* **193**, 39-52 (2008).

31. M. Nayak, E. Asphaug, Sesquinary catenae on the martian satellite Phobos from reaccretion of escaping ejecta. *Nature Communications.* **7**, 12591 (2016).

32. West, B. Knowles, E. Birath, S. Charnoz, D. Di Nino, M. Hedman, P. Helfenstein, A. McEwen, J. Perry, C. Porco, J. Salmon, H. Throop, D. Wilson, In-flight calibration of the *Cassini* imaging science sub-system cameras. *Planet. and Space Sci.* **58,** 1475-1488 (2010).

33. P. C. Thomas, M. Tiscareno, P. Helfenstein, "The Inner Small Satellites of Saturn and Hyperion." in *Enceladus and the Icy Moons of Saturn*, P. Schenk, R.Clark, C. Howett, A. Verbiscer, H. Waite, Eds. (University of Arizona, 2018).

34. R. M. E. Mastrapa, R. H. Brown, Ion irradiation of crystalline H2O-ice: Effect on the 1.65-μm band. *Icarus* **183**, 207-214 (2006).

35. R. N. Clark, Water frost and ice - The near-infrared spectral reflectance 0.65-2.5 microns. *J Geophys. Res.* **86,** 3087-3096 (1981).

36. D. P. Hamilton, J. A. Burns, Origin of Saturn's E-ring: Self-sustained, naturally. *Science* **264**, 550-553 (1994).

37. B. J. Buratti, J. A. Mosher, T. V. Johnson, Albedo and color maps of the Saturnian satellites. *Icarus* **87**, 339-357 (1990).

38. A. Verbiscer, R. French, M. Showalter, P. Helfenstein, Enceladus: Cosmic graffiti artist caught in the act. *Science* **315**, 815 (2007).

39. C. C. Porco, Rings of Saturn (R/2006 S 1, R/2006 S 2, R/2006 S 3, R/2006 S 4). *IAU Circ.*, No. 8759, #1 (2006).

40. A. V. Krivov, M. Sremečvić, F. Spahn, V. V. Dikarev, K. V. Kholshevnikov, Impact-generated dust clouds around planetary satellites: spherically symmetric case. *Planetary and Space Science* **51**, 251-269 (2003).

41. F. Spahn, N. Albers, M. Hörning, S. Kempf, A. V. Krivov, M. Makuch, J. Schmidt, M. Seiß, S. Miodrag, E-ring dust sources: Implications from *Cassini*'s dust measurements. *Planet. and Space Science* **54**, 1024-1032 (2006).

42. S. Kempf, N. Altobelli, J. N. Cuzzi, P. R. Estrada, R. Srama, submitted to Nature (2018).

43. H. Krüger, A. V. Krivov, M. Sremčević, E. Grün, Impact-generated dust clouds surrounding the Galilean moons. *Icarus* **164**, 170-187 (2003).

44. J. A. van Allen, B. A. Randall, D. N. Baker, C. K. Goertz, D. D. Sentman, M. F. Thomsen, H. R. Flindt, Pioneer 11 observations of energetic particles in the Jovian magnetosphere. *Science* **188**, 459-462 (1975).

45. F. B. McDonald, A. W. Schardt, J. H. Trainor, If you've seen one magnetosphere, you haven't seen them all - Energetic particle observations in the Saturn magnetosphere. *J. Geophys. Res.* **85**, 5813-5830 (1980).

46. S. M. Krimigis, D. G. Mitchell, D. C. Hamilton, N. Krupp, S. Livi, E. C. Roelof, J. Dandouras, T. P. Armstrong, B. H. Mauk, C. Paranicas, P. C. Brandt, S. Bolton, A. F. Cheng, T. Choo, G. Gloeckler, J. Hayes, K. C. Hsieh, W.-H. Ip, S. Jaskulek, E. P. Keath, E. Kirsch, M. Kusterer, A. Lagg, L. J. Lanzerotti, D. LaVallee, J. Manweiler, R. W. McEntire, W. Rasmuss, Dynamics of Saturn's magnetosphere from MIMI during *Cassini*'s orbital insertion. *Science* **307**, 1270-1273 (2005).

47. E. Roussos, N. Krupp, P. Kollmann, C. Paranicas, D. G. Mitchell, S. M. Krimigis, M. Andriopoulou, Evidence for dust-driven, radial plasma transport in Saturn's inner radiation belts. *Icarus* **274**, 272-283 (2016).

48. J. A. van Allen, Findings on rings and inner satellites of Saturn of Pioneer 11. *Icarus* **51**, 509-527 (1982).

49. H. Cao, C. T. Russell, U. R. Christensen, M. K. Dougherty, M. E. Burton, Saturn's very axisymmetric magnetic field: No detectable secular variation or tilt. *Earth and Planet. Sci. Lett.* **304**, 22-28 (2011).

50. E. Roussos, N. Krupp, T. P. Armstrong, C. Paranicas, D. G. Mitchell, S. M. Krimigis, G. H. Jones, K. Dialynas, N. Sergis, D. C. Hamilton, Discovery of a transient radiation belt at Saturn. *Geophys. Res. Lett.* **35**, 22106 (2008).

51. P. Kollmann, E. Roussos, A. Kotova, C. Paranicas, N. Krupp, The evolution of Saturn's radiation belts modulated by changes in radial diffusion. *Nature Astronomy.* **1**, 872-877 (2017).

52. B. D. Teolis, G. H. Jones, P. F. Miles, R. L. Tokar, B. A. Magee, J. H. Waite, E. Roussos, D. T. Young, F. J. Crary, A. J. Coates, R. E. Johnson, W.-L. Tseng, R. A. Baragiola, *Cassini* finds an oxygen-carbon dioxide atmosphere at Saturn’s icy moon Rhea. *Science* **330**, 1813 (2010).

53. P. Kollmann, E. Roussos, C. Paranicas, N. Krupp, C. M. Jackman, E. Kirsch, K.-H. Glassmeier, Energetic particle phase space densities at Saturn: *Cassini* observations and interpretations. *J. Geophys. Res. (Space Physics)* **116,** A05222 (2011).

54. C. Paranicas, E. Roussos, N. Krupp, P. Kollmann, A. R. Hendrix, T. Cassidy, R. E. Johnson, P. Schenk, G. Jones, J. Carbary, D. G. Mitchell, K. Dialynas, Energetic charged particle weathering of Saturn's inner satellites. *Planet. Space Sci.* **61**, 60-65 (2012).

55. B. H. Mauk, D. G. Mitchell, R. W. McEntire, C. P. Paranicas, E. C. Roelof, D. J. Williams, S. M. Krimigis, A. Lagg, Energetic ion characteristics and neutral gas interactions in Jupiter's magnetosphere. *Journal Geophys. Res. (Space Physics)* **109**, A09S12 (2004).

56. J. F. Cooper, R. E. Johnson, B. H. Mauk, H. B. Garrett, N. Gehrels, Energetic Ion and Electron Irradiation of the Icy Galilean Satellites. *Icarus* **149**, 133-159 (2001).

57. E. Roussos, N. Krupp, C. Paranicas, J. F. Carbary, P. Kollmann, S. M. Krimigis, D. G. Mitchell, The variable extension of Saturn's electron radiation belts. *Planet. Space Sci*. **104**, 3-17 (2014).

58. J. N. Cuzzi, J. A. Burns, Charged particle depletion surrounding Saturn's F ring - Evidence for a moonlet belt? *Icarus* **74**, 284-324 (1988).

59. R. E. Johnson, T. I. Quickenden, Photolysis and radiolysis of water ice on outer solar system bodies. *J. Geophys. Res*. **102**, 10985-10996 (1997).

60. Z. Zhang, A. G. Hayes, M. A. Janssen, P. D. Nicholson, J. N. Cuzzi, I. de Pater, D. E. Dunn, Exposure age of Saturn's A and B rings, and the *Cassini* Division as suggested by their non-icy material content. *Icarus* **294**, 14-42 (2017).

**Table 1: Summary of five "best ever" flybys of Saturn's ring moons during the Ring-grazing Orbits**

| Moon | Semi-major axis ($R_s$) | Rotation rate (days) | Date of flyby | Closest approach (km) | Spatial resolution improvement factor | Best resolution (Imaging; m/pixel) |
|---|---|---|---|---|---|---|
| Pan | 2.22 | 0.575 | 7 March 2017 | **22,247** | 2 | 147 |
| Daphnis | 2.26 | 0.594 | 16 Jan 2017 | **22,336** | >10 | 170 |
| Atlas | 2.29 | 0.602 | 12 April 2017 | **10,848** | 2 | 76 |
| Pandora | 2.35 | 0.629 | 18 Dec 2016 | **22,157** | ~3 | 132 |
| Epimetheus | 2.51 | 0.695 | 30 Jan 2017 | **3,625** | 6 | 36 |

**Table 2: Sizes and mean densities of Saturn's ring moons described in this paper and Janus**

| Object | a, km | b, km | c, km | $R_m$, km | Density, $kgm^{-3}$ | Gravity, $cms^{-2}$ |
|---|---|---|---|---|---|---|
| Pan | 17.3±0.2 | 14.1±0.2 | 10.5±0.7 | 13.7±0.3 | 400±32 | 0.2-1.7 |
| Daphnis | 4.9±0.3 | 4.2±0.8 | 2.8±0.6 | 3.9±0.5 | 274±142 | 0.0-0.4 |
| Atlas | 20.4±0.1 | 17.7±0.2 | 9.3±0.3 | 14.9±0.2 | 412±19 | 0.0-1.7 |
| Pandora | 51.5±0.3 | 39.5±0.3 | 31.5±0.2 | 40.0±0.3 | 509±12 | 2.0-5.9 |
| Epimetheus | 64.8±0.4 | 58.1±0.8 | 53.5±0.4 | 58.6±0.5 | 625±16 | 6.6-10.9 |
| Janus | 101.8±0.9 | 93.0±0.3 | 74.5±0.3 | 89.0±0.5 | 642±10 | 10.9- 16.9 |

Semi-axes are of ellipsoids fit to shape models and rescaled to volume of the model. $R_m$, the mean radius, is the radius of a sphere of equivalent volume.

Masses for Atlas, Pandora and Epimetheus are from (25). Masses of Pan and Daphnis are from (26). For a full table of Saturn's small inner moons see (supplementary materials).